

Article

Nano-Crystalline Mn–Ni–Co–O Thermistor Powder Prepared by Co-Precipitation Method

Duc Thang Le and Jeong Ho Cho *

Electronic Convergence, Korea Institute of Ceramic Engineering and Technology, Jinju 660-031, Republic of Korea

* Correspondence: goedc@kicet.re.kr; Tel.: +82-55-792-2660

Abstract: Here, we demonstrate that nano-sized Mn–Ni–Co–O powder can be prepared at a low temperature via a co-precipitation method. In this work, Mn^{2+} was partially oxidized to Mn^{3+} ions in an aqueous solution by adding an oxidizing agent (H_2O_2). The co-presence of Mn^{2+} and Mn^{3+} cations enabled the precipitated products to be well-crystallized at a calcining temperature as low as 650 °C, forming a pure cubic spinel structure. The pellets fabricated from this calcined powder showed a relative density of up to 97.1% at a moderate sintering temperature of 1100 °C. Moreover, these ceramics exhibited electrical performance suitable for use in industrial thermistors, i.e., a room temperature resistivity (ρ_{25}) of 1232 Ω cm, a thermistor constant ($B_{25/85}$) of 3676 K, and an aging coefficient ($\Delta R/R$) of 1.43%. High sintering activity as well as the excellent electrical properties of the ceramics was attributed to the fine-sized particles of the synthesized powder.

Keywords: calcination; cubic spinel phase; low temperature; manganese oxide; NTCR thermistor; sintering

1. Introduction

Negative temperature coefficient of resistance (NTCR) nickel manganite oxide ceramics have been widely used for the production of thermistors owing to their excellent temperature sensitivity and cost-effectiveness [1–3]. These materials are absolutely lead-free, and are thus friendly to humans and environment, making them eligible for full RoHS compliance. With a general formula AB_2O_4 (A: tetrahedral and B: octahedral sites), the electrical conductivity of nickel manganite ceramics is commonly assigned to the electron hopping mechanism between the Mn^{3+} and Mn^{4+} states at the octahedral sites, described by the Arrhenius equation [2–7]: $\rho(T) = \rho_0 \exp(E_a/k_B T)$, where ρ_0 is the resistivity at an infinite temperature, T is the absolute temperature, k_B is the Boltzmann constant, and E_a is the activation energy for the hopping process. In practice, the NTCR thermistor response is typically determined by room temperature (RT) resistivity (ρ_{25}) and thermal sensitivity (usually defined as $B_{25/85}$).

The electrical properties of the spinel nickel manganite ceramics are strongly affected by imperfections, that cause changes in the distribution of cations in the spinel lattices. Therefore, to alter ρ_{25} and $B_{25/85}$, the ceramic compositions have been modified (doping/substituting) with various transition metal ions [1,3,5]. Previous investigations have stated that cobalt (Co) is one the most effective ions for fine-tuning the conductivity without much degradation of temperature sensitivity [1,4–9]. Furthermore, incorporating Co was also demonstrated to improve the electrical stability of the nickel manganites [10,11]. Accordingly, Mn–Ni–Co–O ceramics have attracted intensive attention for industrial thermistors.

NTCR thermistors are typically fabricated by sintering powders at high temperatures, which is known as a grain-growth-induced densification process, driven by atomic diffusion in the solid state under thermal energy. Therefore, the characteristics of the powder particles, such as their morphology, crystal structure, chemical homogeneity, and uniformity, play important roles in sintering, as well as the output performance of the resulting ceramics. It has been reported that the use of coarse particles results in a network of pores, while fine-sized particles promote a much better sintering activity, owing to an increase in their surface



Citation: Le, D.T.; Cho, J.H.

Nano-Crystalline Mn–Ni–Co–O Thermistor Powder Prepared by Co-Precipitation Method. *Powders* 2023, 2, 47–58. <https://doi.org/10.3390/powders2010004>

Academic Editor: Paul F. Luckham

Received: 31 October 2022

Revised: 30 December 2022

Accepted: 5 January 2023

Published: 12 January 2023



Copyright: © 2023 by the authors. Licensee MDPI, Basel, Switzerland. This article is an open access article distributed under the terms and conditions of the Creative Commons Attribution (CC BY) license (<https://creativecommons.org/licenses/by/4.0/>).

free energy [12]. For nickel manganite-based compounds, high performance thermistors are commonly achieved by the use of powders with: (i) fine-sized particles and (ii) cubic spinel phase [13].

To prepare spinel powders, a heat treatment process known as calcination is required, as a prerequisite for crystallization. Although nickel manganite-based powders have been prepared by different methods with various experimental conditions [14–16], the pure cubic spinel phase typically occurs only at temperatures above 750 °C [17]. However, at such high temperatures, the calcination commonly causes the primary particles to become oxide particles of a much larger size, up to several micrometers [8,18,19]. To reduce the particle size, most researchers have employed ball milling as an additional mechanical activation step, after calcinations [13,14,18–22]. They were successful in the fabrication of small-sized particles which enhances the sinterability. However, the use of a mechanical process has disadvantages, notably with controlling the morphology, uniformity, as well as the size distribution and reproducibility. Thus, synthesizing nickel manganite powders with a single spinel phase, while imposing the requirement of keeping fine particles, remains a challenge.

In this light, we considered that the main reason for the large-sized powders is the growth driven by thermal energy during calcination. Therefore, a reduction in calcining temperature may offer a possible approach to achieving fine particles. Recently, we demonstrated that nano-sized cubic spinel Mn–Ni–Cu–O powders can be synthesized by a co-precipitation method [23]. The key point is that Mn³⁺ cations were created during preparation, which were then absorbed into the solid materials. The pre-existence of Mn³⁺ cations enabled the crystallization at a temperature as low as 300 °C. The aim of the present study is to prepare new NTCR materials with relatively low resistivities and high sensitivities. We thus sought to extend the co-precipitation technique to synthesize Mn–Ni–Co–O powder in a stepwise manner. Particularly, the targeted Mn_{1.5}Co_{0.6}Ni_{0.9}O₄ powder was produced from a chloride solution. The phase and morphology of the collected powder were characterized with respect to the calcining temperature. Moreover, the sintering activity and electrical property of the resulting bulk ceramics were reported.

2. Materials and Methods

A schematic of the co-precipitation route used to synthesize thermistor materials in the present work is shown in Figure 1. The solution was prepared in a way similar to that used for the preparation of Mn–Ni–Cu–O powder [23]. MnCl₂·4H₂O, NiCl₂·6H₂O, and CoCl₂·6H₂O (99.99%, Sigma–Aldrich, MA, USA) were used as starting materials. After weighing, a mixed compound with a molar ratio of Mn:Ni:Co = 1.5:0.6:0.9 was dissolved in D.I water to form a 0.1 M solution in a flat bottom flask. NH₄Cl was added and the mixture was stirred using a magnetic stirrer for 1 h. Then, ammonia (NH₃·H₂O) was slowly added to obtain a pH of 7.05. When the pH value was stable, a H₂O₂ (5 mM) solution was introduced, while the solution was continuously stirred for another 1 h. The pH value was further increased up to 9.00 and this state was maintained for an extra 30 min. The resulting brown solution was transferred into a petri dish and was then heated to 120 °C at 10 °C/h in an oven. The solid product was collected and ground, following by calcination in air for 2 h.

The product (in powder form) calcined at 650 °C was selected to blend with polyvinyl alcohol (PVA), followed by cold pressing into circular disks with 12 mm diameter and 2 mm thickness, under a pressure of 200 MPa. After de-binding at 650 °C (2 h), the disks were sintered in air at various temperatures (900–1100 °C) in covered alumina crucibles for 2 h.

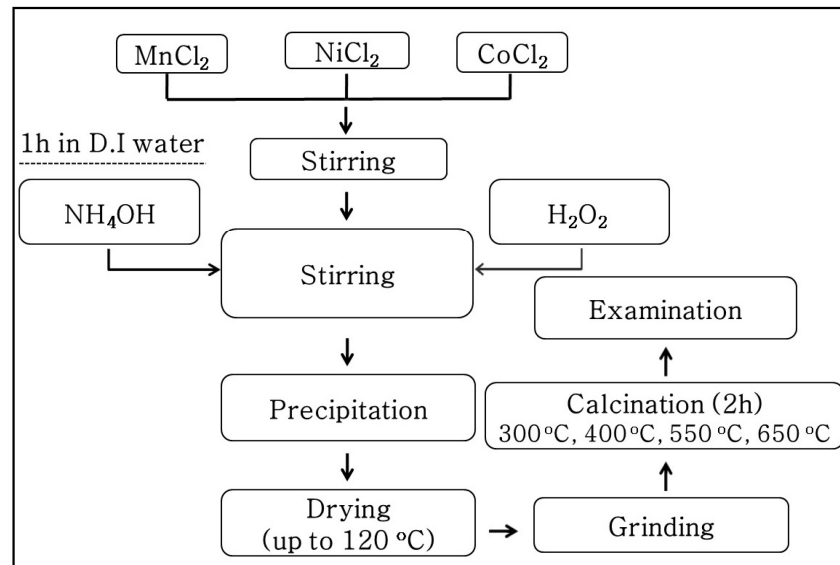


Figure 1. Flowchart for Mn–Ni–Co–O powder preparation from a chloride solution.

According to the Archimedes method, an object will be buoyed up when immersed in fluid by a force that is equal to the weight of the fluid displaced. Therefore, the density of the sintered ceramics can be determined by the following equation: Density (g/cm^3) = $(W_0 \times r_f)/(W_0 - W_i)$, where W_0 and W_i are the weight of the sample in air and in fluid, and r_f is the density of the fluid. The powder surface morphology was examined by field-emission scanning electron microscopy (FE-SEM, 6700F, JEOL, Tokyo, Japan) and transmission electron microscopy (TEM, JEM 2100, JEOL, Tokyo, Japan). The crystal structure of the calcined powders and sintered pellets was analyzed by X-ray diffractometer (XRD, Rigaku, Japan). Inductively coupled plasma optical emission spectroscopy (5110 ICP-OES, Agilent, Santa Clara, CA, USA) was used to characterize chemical composition. Change in valence states of manganese was confirmed by X-ray photoelectron spectroscopy (XPS) using a VG ESCA 3000 system (Microtech, Maidehead, UK). To measure electrical properties, the disks were polished to 1.0 mm in thickness, and silver paste was printed to both surfaces. Afterwards, they were cured at 700 °C for 10 min. These electroded specimens were held in a silicon oil bath, where a digital thermometer was used to measure temperature. Change in electrical resistance with temperature was detected by a digital multimeter (Fluke 45, 8808A, WA, USA). The $B_{25/85}$ constant was calculated by the equation $B_{25/85} = 1778 \times (\ln R_{25} - \ln R_{85})$, where R_{25} and R_{85} are the bulk specific resistances (Ω) at 25 °C (298 K) and 85 °C (358 K), respectively. The aging coefficient was examined by the relative change in resistance $\Delta R/R = (R - R_0)/R_0 \times 100\%$, where R_0 and R are the resistances at 298 K before and after aging 500 h in air at 150 °C. The values of ρ_{25} , $B_{25/85}$, and $\Delta R/R$ were the averages of four tested pellets.

3. Results and Discussion

Figure 2 shows an FE-SEM image of the as-synthesized powder, observed after drying at 120 °C. It is seen that the primary particles of the powder are quite similar, with tens of nanometers in size. However, some of them have agglomerated and form large, densified aggregates with a larger size up to a few hundred nanometers. This can be understood as a common phenomenon that occurs to minimize the surface free energy of these particles [13].

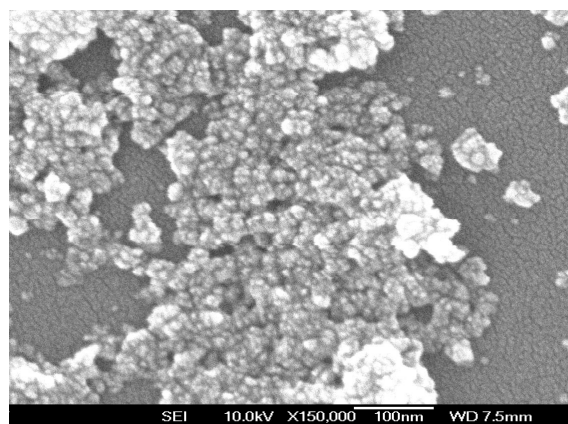


Figure 2. FE-SEM photograph of the as-prepared powder.

The XRD patterns of the powder calcined at various temperatures are depicted in Figure 3. As expected, distinct peaks appear in the powder calcined at 300 °C, which are in accordance with those of the standard $Fd\bar{3}m$ space group cubic spinel NiMn_2O_4 ceramics (JCPDS card No. 84-0542). The broadening of the preferential orientation (311) peak implies that the material exhibits a low crystallinity degree [24]. As the calcining temperature increases, sharper peaks with higher intensity and less humps are observed. These changes in XRD patterns demonstrate the growth of crystallites, which is further confirmed by an increase in crystallite size, shown in Table 1. Notably, at 650 °C, a well-crystallized pure single phase was found, indicating the completion of phase formation. It has been reported that there is a phase decomposition into NiMnO_3 and Mn_2O_3 in the temperature range 400–750 °C, and therefore stoichiometric spinel NiMn_2O_4 -based compounds can be achieved only at temperatures higher than 750 °C [15,25]. Nevertheless, except for an increase in intensity, Figure 3 shows an unchanged XRD characteristic within the studied temperature range (300–650 °C). No dissociation and/or secondary phases are detected, indicating an unchanged cubic spinel structure phase for the present Mn–Ni–Co–O solid products.

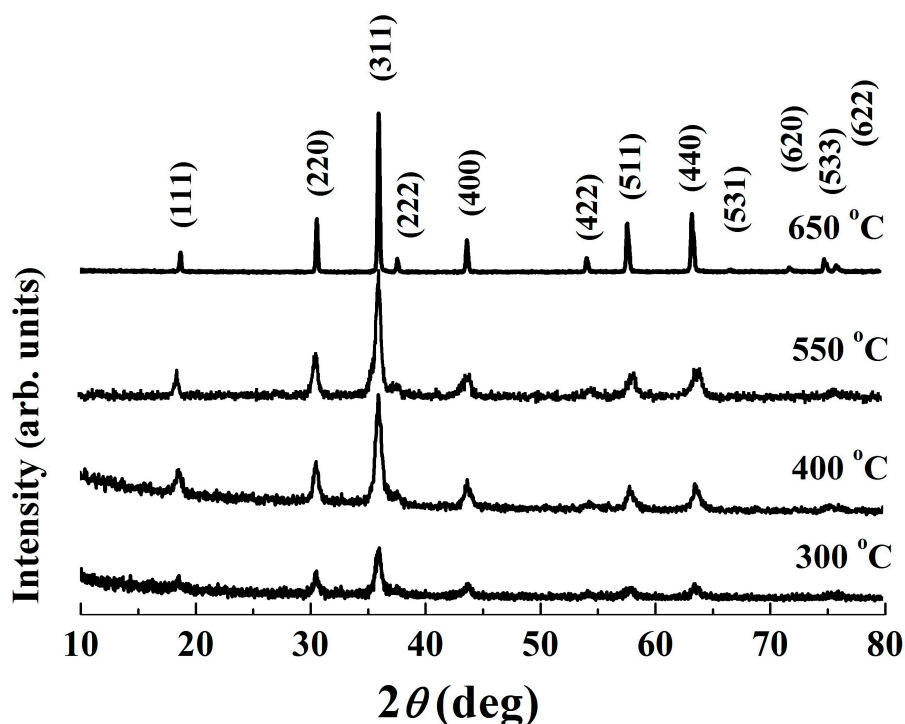
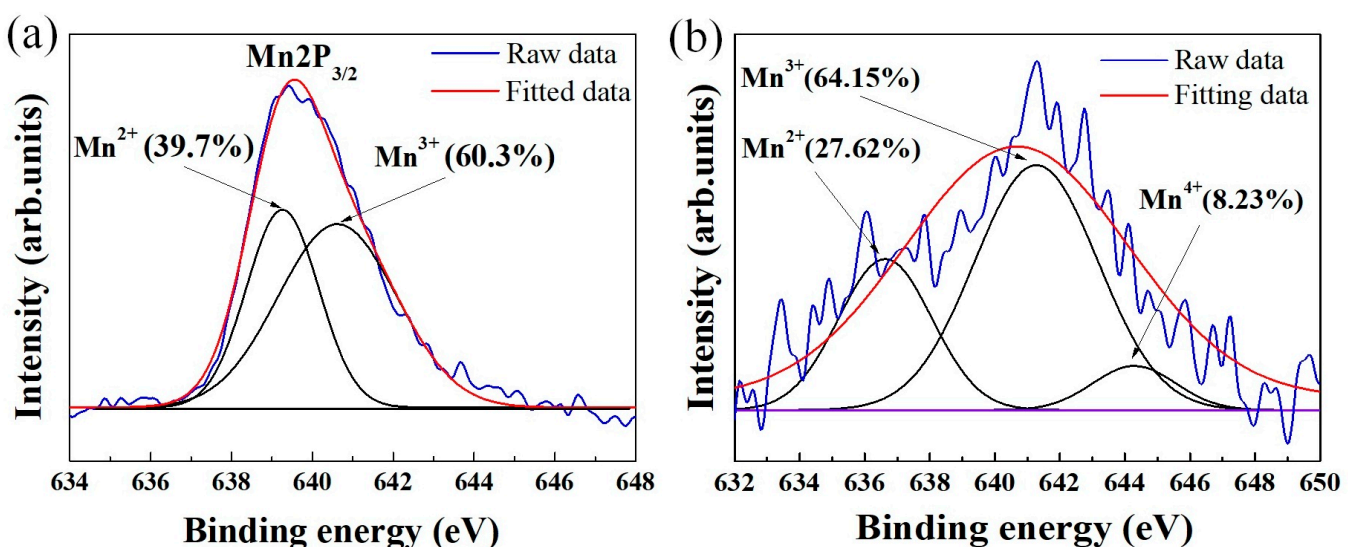


Figure 3. XRD patterns of calcined powders.

Table 1. Crystallite size of calcined powders, calculated by using Scherrer's formula [26,27].

Sample No	Calcining Temperature, °C	Crystallite Size, nm
1	300	6.65
2	400	10.34
3	550	14.56
4	650	19.54

It has been demonstrated that the use of solution routes such as co-precipitation can reduce the crystallization temperature of powders due to the homogeneous mixing of the starting components [28]. Nevertheless, we think that chemical homogeneity alone cannot sufficiently account for a crystallization temperature as low as 300 °C. Figure 4a presents the results of high-resolution XPS Mn2p_{3/2} analysis of the pristine powder (Figure 2). Through Gaussian–Lorentzian curve fitting, the Mn2p_{3/2} spectra can be split into two peaks in the binding energy range 634–648 eV, which can be assigned to the Mn²⁺ and Mn³⁺ oxidation states [29]. As expected, both 2+ and 3+ valence states of manganese are found, implying that Mn²⁺ was partially oxidized to Mn³⁺ during synthesis. Commonly, due to the occurrence of Mn²⁺ → Mn³⁺ oxidation reactions (driven by heat energy), there is a difference in the Mn³⁺/Mn²⁺ ratio between the pristine and heated states. However, the XPS analysis for powder fired at 300 °C (Figure 4b) shows that the Mn³⁺/Mn²⁺ ratio does not change significantly after calcination. This is likely due to the high portion of Mn³⁺ ions (60.3%) pre-existing in the as-prepared material (Figure 4a), which causes only a few Mn²⁺ → Mn³⁺ conversions to happen for acquiring the spinel phase. Consequently, the required thermal energy budget for crystallization is lower. We therefore theorize that the major factors responsible for the formation of the spinel at the critical temperature of 300 °C are the co-existence of Mn²⁺ and Mn³⁺ and the chemical homogenous dispersion. We also suggest that due to the suppression of Mn²⁺ → Mn³⁺ conversion in the manganite, no secondary phases (NiMnO₃ and α-Mn₂O₃) were formed [30], which may be a possible reason for the stable spinel phase shown in Figure 3. In addition, Figure 4b indicates that Mn⁴⁺ cations are found in the powder calcined at 300 °C. This result illustrates the conversion of Mn³⁺ to Mn⁴⁺ even at only 300 °C. For nickel manganite-based materials, the formation of Mn⁴⁺ ions is the critical factor which enables electrical conduction via the hopping mechanism [2–7,20–23].

**Figure 4.** XPS spectra of Mn2p_{3/2} for different powder states (a) as-prepared and (b) calcined at 300 °C.

The calcination process commonly causes a growth and/or a morphological change in the synthesized particles. In our case, the powder fired at 650 °C shown in Figure 5a looks quite uniform over the FE-SEM scan area. The magnified FE-SEM image (insert of Figure 5a) shows a spherical shape for particles, with a majority at approximately 100–120 nm in size. TEM observation (Figure 5b) confirmed that these particles are not larger than 150 nm. Clearly, the particles are enlarged after the heat treatment; however, such particles are much smaller than those prepared by most other recent techniques [8,12–14,21,22,26,31]. The fine size of the calcined powder can be attributed to the moderate firing temperature of only 650 °C. Otherwise, the uniformity and narrow particle size distribution may relate to the fact that no mechanical impacts were involved in the proposed process.

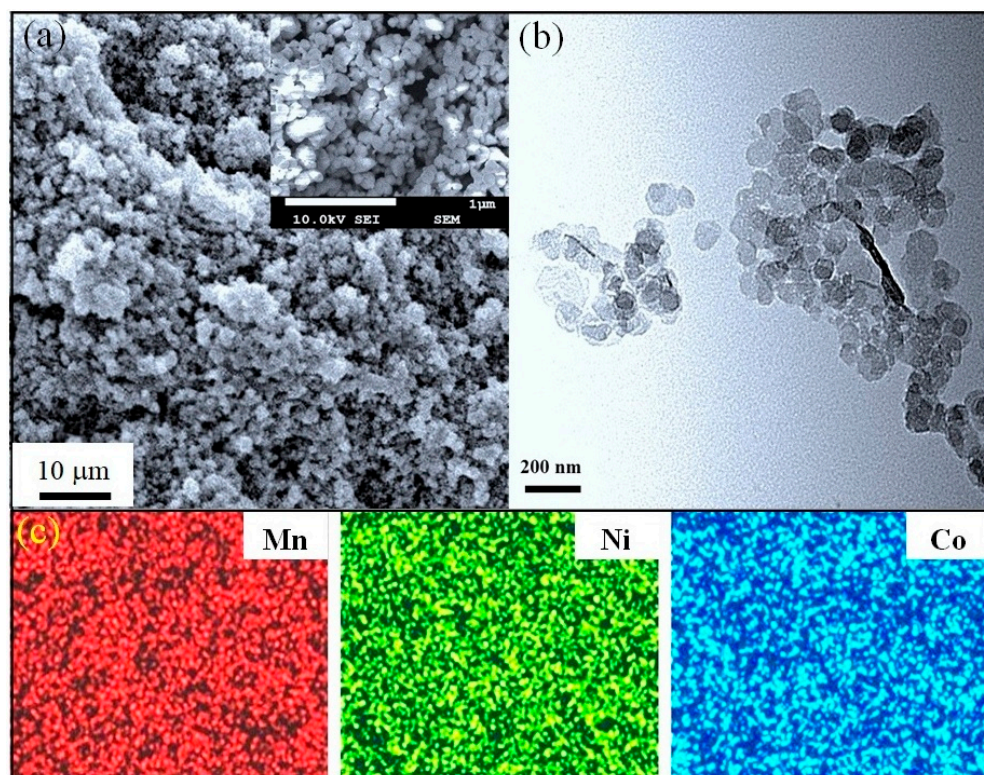


Figure 5. (a) FE-SEM, (b) TEM and (c) EDS mapping (Mn, Ni, and Co) images of the powder calcined at 650 °C. Inset in (a): magnified FE-SEM image shows quite uniform particles with a spherical shape.

The chemical compositions of the powder in the as-prepared and 650 °C calcined states were characterized using inductively coupled plasma (ICP) and the results are shown in Table 2. It is found that the ratios of the constituent elements (Mn:Ni:Co) measured in these different states are similar to those in the initial solution. The ICP results thus suggest that both the precipitate collection and calcining processes did not noticeably affect the chemical composition. Moreover, all elements were homogeneously distributed over the powder, as can be observed from the elemental mapping SEM image in Figure 5c. This result is reasonable due to the fact that a homogeneous mixture of starting materials can be easily obtained in solution processes. Due to the combined advantages of a cubic spinel structure, fine-sized particles, and uniformity, it is possible to expect good sintering behavior and electrical performance for the resulting ceramics.

Table 2. Chemical compositions of synthesized powder in different states.

Metal Elements	Chemical Composition		
	Solution	As-Prepared	Calcined at 650 °C
Mn	1.50	1.52	1.54
Ni	0.60	0.57	0.59
Co	0.90	0.91	0.87

Generally, the crystallization degree of calcined powders strongly affects the electrical characteristics of the resulting ceramics. In the present work, although the prepared Mn–Ni–Co–O material was started to crystallize at 300 °C, the formation of the cubic spinel structure (from amorphous phase) was only completed at 650 °C (Figure 3). Therefore, for further investigations of sinterability and electrical properties, the powder calcined at 650 °C was selected to form into circular bulks and sintered in air for 2 h. Figure 6 shows the shrinkage of the ceramics observed as a function of sintering temperature. It was found that the linear shrinkage rapidly increased from 8.2% to 12.7% as the temperature increased from 900 °C to 1000 °C. This noticeable change in shrinkage is in agreement with the results of Vidales et al. [8] for Mn–Ni–Co–O ceramics prepared via the same route. Because of the large shrinkage rate, a remarkable increase in relative density (RD) of up to 92.3% is observed, as shown in Figure 6 (insert). At temperatures above 1000 °C, the shrinkage tendency is retained but with a reduced rate. A RD of 97.1% is achieved at 1100 °C, where the final linear shrinkage reaches 14.3%. In fact, the ceramics gave an RD value of nearly 97.5% when the sintering duration was held for 6 h.

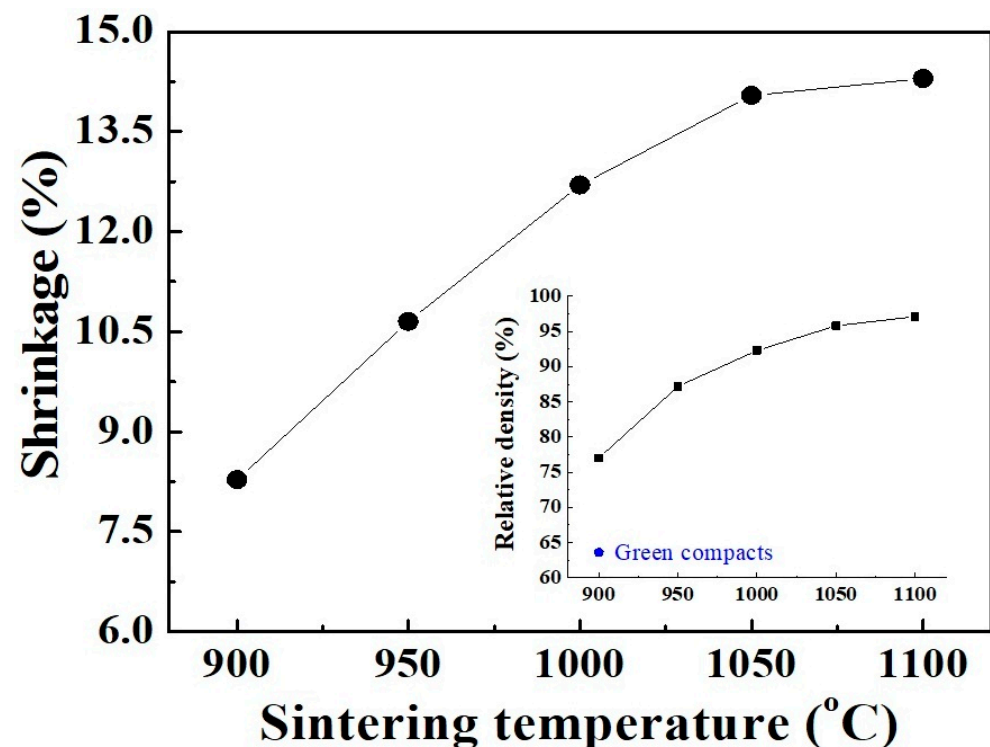
**Figure 6.** Shrinkage of ceramic pellets, examined as a function of the sintering temperature. The inset shows the relative density (RD) of the ceramics.

Figure 7 shows FE-SEM images of the surface of three pellets that were sintered at different temperatures. It can be clearly seen that the specimen fired at 900 °C exhibits many large pores. However, only small closed pores are visible on the surface of the one sintered at 1000 °C, revealing a denser structure with less porosity. In the sample heated at 1100 °C, the pores are almost eliminated. The bulk looks quite dense and

homogenous. Otherwise, within the sintering temperature range, there is an increase in the average grain size (AGS) from 1.04 to 1.82 μm . These changes in microstructure explain the promotion of densification, as well as the RD increase with respect to sintering temperature shown in Figure 6. It should be noted that the sintering temperature of 1100 $^{\circ}\text{C}$, which enabled an RD value larger than 97%, is lower than those reported for most conventional ceramics that possess the same RD level [32–34]. On the other hand, at the sintering temperature of 1100 $^{\circ}\text{C}$, the pure cubic spinel structure is retained without any other secondary phase being detected, even though the dwell time was extended to 6 h (Figure 8). This means that no phase transformation and/or segregation took place during sintering. Therefore, it is worth noting that the sintering at such a low temperature (1100 $^{\circ}\text{C}$) prevents decomposition reactions (into rock salt NiO phase), that are commonly observed at high temperatures [13,17,26,35]. These are consistent with the previous results [12,15,23], which indicate that the formation of the secondary phase can be suppressed by sintering at a low temperature. We suggest that the fine size of the calcined powder (Figure 5) is mainly responsible for the good densification of the ceramics because it allows a high possibility for particles to fill any spaces/voids in the bulk volume. This is confirmed by the result shown in Figure 6 (insert), where the RD of the green compact was found to be as high as 63.2%. In addition, because of having large free surface energy [12], more contacts and reactions among particles can be created, which enables the diffusion process in the solid state during sintering.

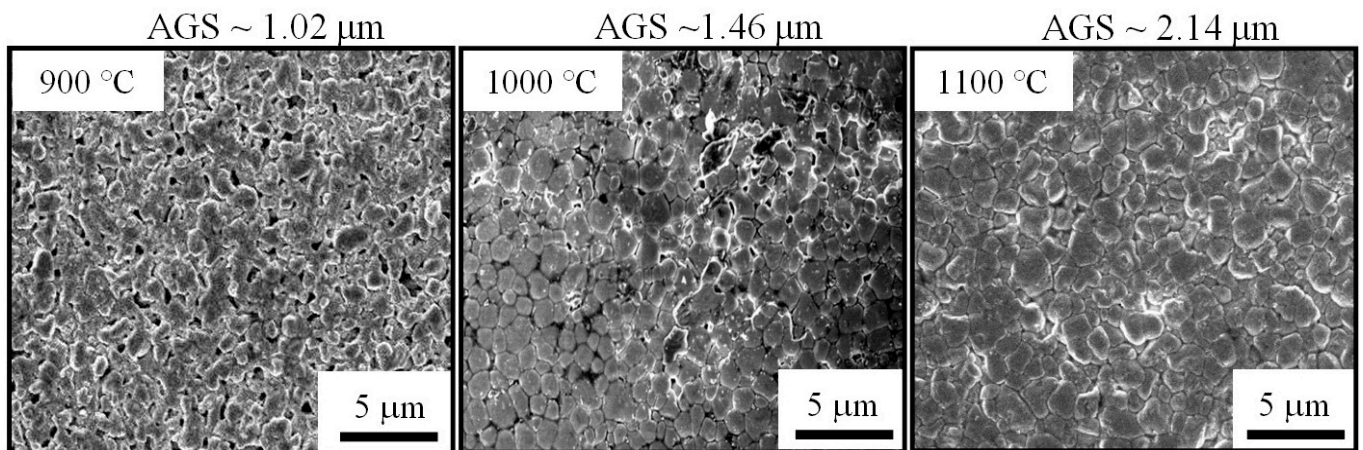


Figure 7. Surface FE-SEM micrographs of sintered ceramics.

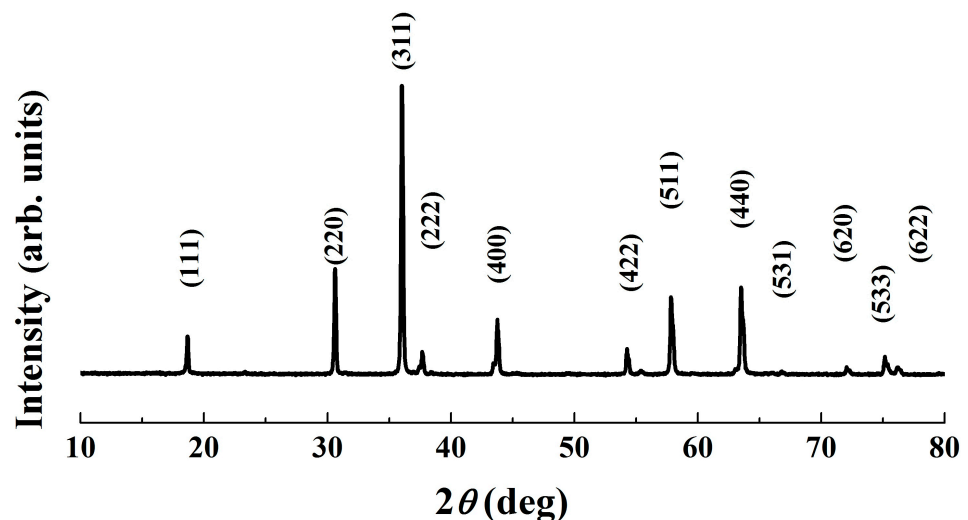


Figure 8. XRD patterns of bulk ceramic sintered at 1100 $^{\circ}\text{C}$ for 6 h.

Measurement of the electrical resistivity–temperature (ρ – T) dependence was carried out on pellets sintered at 1100 °C, and the results are presented in Figure 9a. It is found that as the testing temperature increased (295–391 K), the resistivity progressively decreased. Moreover, the inset illustrates a nearly linear relationship between $\ln(\rho/T)$ and $1000/T$. Obviously, Figure 9a reveals a typical NTCR characteristic of nickel manganites that can be conducted to the hopping mechanism presented by the Arrhenius model [2–5,36,37]. The thermistor parameters of the sintered samples are listed in Table 3. The ρ_{25} and $B_{25/85}$ were calculated to be 1232 Ω cm and 3676 K, respectively, which are suitable for use in low-resistance thermistors. These parameters are comparable to those of conventional Mn–Ni–Co–O ceramics sintered at 1200 °C and above [9,36,37]. Otherwise, to gain more information about the electrical properties, we provide the ρ – T tested results for the samples derived from powders calcined at 300 °C, 400 °C, and 550 °C, as shown in Figure 9b. It is found that under the same sintering conditions (1100 °C, 2 h), the NTCR behavior is also revealed for all these ceramics, however, with much higher ρ_{25} (Table 3). These results confirm that the electrical conductivity is worse when using incomplete crystallization powders.

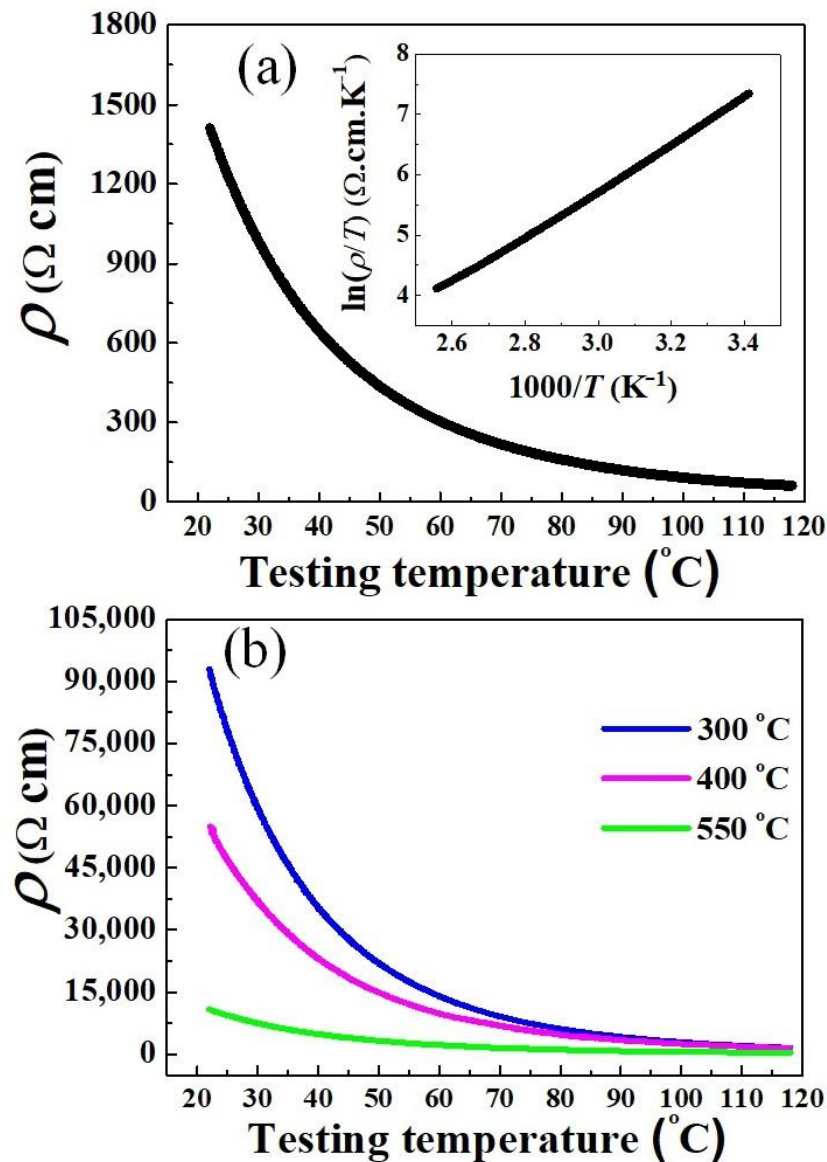


Figure 9. Resistivity–temperature (ρ – T) dependence of sintered ceramics (1100 °C, 2 h), produced from powders calcined at (a) 650 °C, and (b) lower than 650 °C. The insert in (a) shows the plot of $\ln(\rho/T)$ versus $(1000/T)$.

Table 3. The electrical properties of ceramics sintered at 1100 °C.

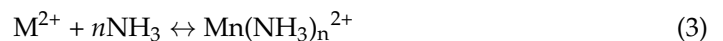
Sample No	Calcining Temperature, °C	ρ_{25} (Ω cm)	$B_{25/85}$ (K)	$\Delta R/R$ (%)
1	300	$77,379 \pm 248$	–	–
2	400	$46,316 \pm 159$	–	–
3	550	9873 ± 72	–	–
4	650	1232 ± 17	3676 ± 28	1.43 ± 0.12

The drift in resistance ($\Delta R/R$) due to aging and/or long time operation, the so-called aging coefficient, is also vital for practical applications. The $\Delta R/R$ describes the electrical stability, and it should be as low as possible to maintain external responses [38]. Table 3 also shows an average $\Delta R/R$ value of 1.43% after the ceramics were aged for 500 h, demonstrating extremely high stability. It has been reported that aging behavior is primarily caused by the oxidation reactions during metallization [39,40]. Therefore, the little change in resistance here can be supported by the dense and fine-grained microstructure shown in Figure 7 (AGS~1.82 μ m), which suppresses oxygen adsorption, leading to more stable spinel lattices [41].

It should be again mentioned that the oxidation of Mn^{2+} to Mn^{3+} ions was noted as the key factor, which induces the formation of cubic spinel structure at low temperatures. For better understanding, the formation mechanism of present Mn–Ni–Co–O powders was proposed as follows:

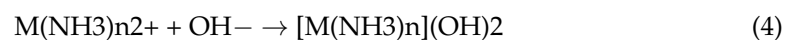


The metal amine complexes ($M(NH_3)_n^{2+}$) are formed as follows:



M–Mn, Ni, and Co

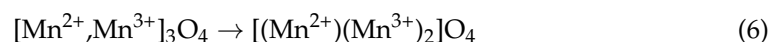
The metal amine complexes then combine with OH^- groups:



Once the oxidizing agent (H_2O_2) is added, some M^{2+} ions are oxidized to form M^{3+} :



Finally, under thermal energy of calcination, the spinel phase is formed:



4. Conclusions

In this work, the cubic spinel nano-sized powder was successfully produced via a simple solution method, from a mixed chloride aqueous solution. The addition of H_2O_2 induced the partial oxidation of Mn^{2+} to Mn^{3+} ions in solution, which was noted as the key factor that enables the crystallization to begin at 300 °C. Notably, powder calcined at 650 °C possessed quite uniform particles with a size smaller than 150 nm, which promoted high densification in the resulting ceramics. As a result, a relative density (RD) of 97.1% was obtained for pellets sintered at 1100 °C, while maintaining a pure cubic spinel phase. Furthermore, these ceramics exhibited a typical NTCR behavior, with average ρ_{25} , $B_{25/85}$, and $\Delta R/R$ of 1232 Ω cm, 3676 K, and 1.43%, respectively. The results demonstrate a feasible approach for the fabrication of spinel nano-sized thermistor powders.

Author Contributions: Conceptualization, D.T.L. and J.H.C.; methodology, D.T.L.; formal analysis, D.T.L. and J.H.C.; investigation, D.T.L. and J.H.C.; resources, J.H.C.; data curation, D.T.L.; writing—original draft preparation, D.T.L.; writing—review and editing, J.H.C.; supervision, J.H.C. All authors have read and agreed to the published version of the manuscript.

Funding: This research was financially supported by a grant from the R&D program for Material/Parts Technology Development funded by the Ministry of Trade, Industry and Energy, Republic of Korea, grant number, 20016729.

Institutional Review Board Statement: Not applicable.

Informed Consent Statement: Not applicable.

Data Availability Statement: The data presented in this study are available on request from the corresponding author. The data are not publicly available due to privacy.

Conflicts of Interest: The authors declare no conflict of interest.

References

1. Price, B.Y.; Hardal, G. Electrical properties of $\text{Ni}_{0.5}\text{Co}_{0.8}\text{Mn}_{1.7}\text{O}_4$ and $\text{Ni}_{0.5}\text{Co}_{1.1}\text{Mn}_{1.4}\text{O}_4$ negative temperature coefficient ceramics doped with B_2O_3 . *J. Mater. Sci. Mater. Electron.* **2021**, *32*, 8983–8990. [[CrossRef](#)]
2. Feteira, A. Negative Temperature Coefficient Resistance (NTCR) Ceramic Thermistors: An Industrial Perspective. *J. Am. Ceram. Soc.* **2009**, *92*, 967–983. [[CrossRef](#)]
3. Schulze, H.; Li, J.; Dickey, E.C.; Trolier-McKinstry, S. Synthesis, Phase Characterization, and Properties of Chemical Solution-Deposited Nickel Manganite Thermistor Thin Films. *J. Am. Ceram. Soc.* **2009**, *92*, 738–744. [[CrossRef](#)]
4. Sachse, H.F. *Semiconducting Temperature Sensors and Their Applications*; Wiley: New York, NY, USA, 1975.
5. Metz, R. Electrical properties of N.T.C. thermistors made of manganite ceramics of general spinel structure: $\text{Mn}_{3-x-x'}\text{M}_x\text{N}_{x'}\text{O}_4$ ($0 \leq x + x' \leq 1$; M and N being Ni, Co or Cu). Aging phenomenon study. *J. Mater. Sci.* **2000**, *35*, 4705–4711. [[CrossRef](#)]
6. Luo, W.; Yao, H.M.; Yang, P.H.; Chen, C.S. Negative temperature coefficient material with low thermal constant and high resistivity for low-temperature thermistor applications. *J. Am. Ceram. Soc.* **2009**, *92*, 2682–2686. [[CrossRef](#)]
7. Jadhav, R.N.; Mathad, S.N.; Puri, V. Studies on the properties of $\text{Ni}_{0.6}\text{Cu}_{0.4}\text{Mn}_2\text{O}_4$ NTC ceramic due to Fe doping. *Ceram. Int.* **2012**, *38*, 5181–5188. [[CrossRef](#)]
8. Vidales, J.L.M.; Garcia-Chain, P.; Rojas, R.M.; Vila, E.; Garcia Martinez, O. Preparation and characterization of spinel type Mn–Ni–Co–O negative temperature coefficient ceramic thermistors. *J. Mater. Sci.* **1998**, *33*, 1491–1496. [[CrossRef](#)]
9. Zhao, Y.; Xie, Y.; Yao, J.; Tang, X.; Wang, J.; Chang, A. NTC thermo-sensitive ceramics with low B value and high resistance at low temperature in Li-doped $\text{Mn}_{0.6}\text{Ni}_{0.9}\text{Co}_{1.5}\text{O}_4$ system. *J. Mater. Sci. Mater. Electron.* **2020**, *31*, 1403–1410. [[CrossRef](#)]
10. Park, K.; Lee, J.K. Mn–Ni–Co–Cu–Zn–O NTC thermistors with high thermal stability for low resistance applications. *Scr. Mater.* **2007**, *57*, 329–332. [[CrossRef](#)]
11. Liu, X.; Wang, J.; Hu, Z.; Yao, J.; Chang, A. Effect of Fe addition on microstructure and electrical properties of $\text{Co}_{1.5}\text{Mn}_{1.5-x}\text{Fe}_x\text{O}_4$ ($0.2 \leq x \leq 1.0$) NTC thermistors. *J. Mater. Sci. Mater. Electron.* **2017**, *28*, 7243–7247. [[CrossRef](#)]
12. Kocjan, A.; Logar, M.; Shen, Z. The agglomeration, coalescence and sliding of nanoparticles, leading to the rapid sintering of zirconia nanoceramics. *Sci. Rep.* **2017**, *7*, 2541. [[CrossRef](#)]
13. Aleksic, O.S.; Nikolic, M.V.; Lukovic, M.D.; Nikolic, N.; Radojic, B.M.; Radovanovic, M.; Djuric, Z.; Mitric, M.; Nikolic, P.M. Preparation and characterization of Cu and Zn modified nickel manganite NTC powders and thick film thermistors. *Mater. Sci. Eng. B* **2013**, *178*, 202–210. [[CrossRef](#)]
14. Fang, D.L.; Wang, Z.B.; Yang, P.H.; Liu, W.; Chen, C.S. Preparation of Ultra-Fine Nickel Manganite Powders and Ceramics by a Solid-State Coordination Reaction. *J. Am. Ceram. Soc.* **2006**, *89*, 230–235. [[CrossRef](#)]
15. Teichman, C.; Töpfer, J. Sintering and electrical properties of Cu-substituted Zn–Co–Ni–Mn spinel ceramics for NTC thermistors thick films. *J. Eur. Ceram. Soc.* **2022**, *42*, 2261–2267. [[CrossRef](#)]
16. Uppuluri, K.; Szwagierczak, D. Fabrication and characterization of screen printed NiMn_2O_4 spinel based thermistors. *Sens. Rev.* **2022**, *42*, 177–186. [[CrossRef](#)]
17. Drouet, C.; Laberty, C.; Fierro, J.L.G.; Alphonse, P.; Rousset, A. X-ray photoelectron spectroscopic study of non-stoichiometric nickel and nickel-copper spinel manganites. *Int. J. Inorg. Mater.* **2000**, *2*, 419–426. [[CrossRef](#)]
18. Chanel, C.; Fritsch, S.; Legros, R.; Rousset, A. Controlled Morphology of Nickel Manganite Powders. *Key Eng. Mater.* **1997**, *132*, 109–112. [[CrossRef](#)]
19. Zhang, M.; Li, M.; Zhang, H.; Tuokedaerhan, K.; Chang, A. Synthesis of pilot-scale $\text{Co}_2\text{Mn}_{1.5}\text{Fe}_{2.1}\text{Zn}_{0.4}\text{O}_8$ fabricated by hydrothermal method for NTC thermistor. *J. Alloys Compd.* **2019**, *797*, 1295–1298. [[CrossRef](#)]
20. Savić, S.M.; Mančić, L.; Vojisavljević, K.; Stojanović, G.; Branković, Z.; Aleksić, O.S.; Branković, G. Microstructural and electrical changes in nickel manganite powder induced by mechanical activation. *Mater. Res. Bull.* **2011**, *46*, 1065–1071. [[CrossRef](#)]
21. Zheng, C.H.; Fang, D.L. Preparation of ultra-fine cobalt-nickel manganite powders and ceramics derived from mixed oxalate. *Mater. Res. Bull.* **2008**, *43*, 1877–1882. [[CrossRef](#)]

22. Fang, D.L.; Lee, C.G.; Koo, B.H. Preparation of Ultra-Fine FeNiMnO₄ Powders and Ceramics by a Solid-State Coordination Reaction. *Met. Mater. Int.* **2007**, *13*, 165–170. [[CrossRef](#)]
23. Le, D.T.; Ju, H. Solution Synthesis of Cubic Spinel Mn–Ni–Cu–O Thermistor Powder. *Materials* **2021**, *14*, 1389. [[CrossRef](#)] [[PubMed](#)]
24. Park, K.R.; Mhin, S.; Han, H.; Kim, K.M.; Shim, K.B.; Lee, J.I.; Ryu, J.H. Electrical properties of Fe doped Ni–Mn–Co–O cubic spinel nanopowders for temperature sensors. *J. Ceram. Process. Res.* **2017**, *18*, 247–251.
25. de Gyoryfalva, G.D.C.C.; Reaney, I.M. Decomposition of NiMn₂O₄ spinels. *J. Mater. Res.* **2003**, *18*, 1301–1308. [[CrossRef](#)]
26. Khirade, P.P.; Birajdar, S.D.; Raut, A.; Jadhav, K. Multiferroic iron doped BaTiO₃ nanoceramics synthesized by sol–gel auto combustion: Influence of iron on physical properties. *Ceram. Int.* **2016**, *42*, 12441–12451. [[CrossRef](#)]
27. Ahsan, M.; Irshad, M.; Fu, P.F.; Siraj, K.; Raza, R.; Javed, F. The effect of calcination temperature on the properties of Ni–SDC cermet anode. *Ceram. Int.* **2019**, *46*, 2780–2785. [[CrossRef](#)]
28. Lee, B.W. Preparation and characterization of spinel LiCo_xMn_{2–x}O₄ by oxalate precipitation. *J. Power Sources* **2002**, *109*, 220–226. [[CrossRef](#)]
29. Tan, B.J.; Klabunde, K.J.; Sherwood, P.M. XPS Studies of Solvated Metal Atom Dispersed (SMAD) Catalysts. Evidence for Layered Cobalt–Manganese Particles on Alumina and Silica. *J. Am. Chem. Soc.* **1991**, *113*, 855–861. [[CrossRef](#)]
30. Gao, H.; Ma, C.; Sun, B. Preparation and characterization of NiMn₂O₄ negative temperature coefficient ceramics by solid–state coordination reaction. *J. Mater. Sci. Mater. Electron.* **2014**, *25*, 3990–3995. [[CrossRef](#)]
31. Arinicheva, Y.; Clavier, N.; Neumeier, S.; Podor, R.; Bukaemskiy, A.; Klinkenberg, M.; Roth, G.; Dacheux, N.; Bosbach, D. Effect of powder morphology on sintering kinetics, microstructure and mechanical properties of monazite ceramics. *J. Eur. Ceram. Soc.* **2018**, *38*, 227–234. [[CrossRef](#)]
32. Hardal, G.; Price, B.Y. Influence of nano–sized cobalt oxide additions on the structural and electrical properties of nickel–manganite–based NTC thermistors. *Mater. Technol.* **2016**, *50*, 923–928. [[CrossRef](#)]
33. Park, K.; Kim, S.J.; Kim, J.G.; Nahm, S. Structural and electrical properties of MgO–doped Mn_{1.4}Ni_{1.2}Co_{0.4–x}Mg_xO₄ (0 ≤ x ≤ 0.25) NTC thermistors. *J. Eur. Ceram. Soc.* **2007**, *27*, 2009–2016. [[CrossRef](#)]
34. Irshad, M.; Siraj, K.; Raza, R.; Rafique, M.; Usman, U.; Ain, Q.; Ghaffar, A. Evaluation of densification effects on the properties of 8 mol % yttria stabilized zirconia electrolyte synthesized by cost effective coprecipitation route. *Ceram. Int.* **2021**, *47*, 2857–2863. [[CrossRef](#)]
35. Rong, J.; Zhang, H.; Zhao, P.; Qin, Q.; He, D.; Xie, J.; Ding, Y.; Jiang, H.; Wu, B.; Chang, A. Effect of Zn/Fe co–doping on the microstructure, electrical properties and aging behavior of Co–Mn–Ni–O NTC ceramics. *Appl. Phys. A* **2022**, *128*, 444. [[CrossRef](#)]
36. Price, B.Y.; Hardal, G. Influence of B₂O₃ addition on the electrical and microstructure properties of Ni_{0.5}Co_{0.5}Cu_xMn_{2–x}O₄ (0 ≤ x ≤ 0.3) NTC thermistors without calcination. *J. Mater. Sci. Mater. Electron.* **2016**, *27*, 9226–9232. [[CrossRef](#)]
37. Muralidharan, M.N.; Rohini, P.R.; Sunny, E.K.; Dayas, K.R.; Seema, A. Effect of Cu and Fe addition on electrical properties of Ni–Mn–Co–O NTC thermistor compositions. *Ceram. Int.* **2012**, *38*, 6481–6486. [[CrossRef](#)]
38. Zhao, M.; Chen, W.; Wu, W.; Zhang, M.; Li, Z. Aging characteristic of Cu-doped nickel manganite NTC ceramics. *J. Mater. Sci. Mater. Electron.* **2020**, *31*, 11784–11790. [[CrossRef](#)]
39. Fritsch, S.; Sarrias, J.; Brieu, M.; Couderc, J.J.; Baudour, J.L.; Snoeck, E.; Rousset, A. Correlation between the structure, the microstructure and the electrical properties of nickel manganite negative temperature coefficient (NTC) thermistors. *Solid State Ion.* **1998**, *109*, 229–237. [[CrossRef](#)]
40. Le, D.T.; Cho, J.H.; Ju, H. Electrical properties and stability of low temperature annealed (Zn,Cu) co–doped (Ni,Mn)₃O₄ spinel thin films. *J. Asian Ceram. Soc.* **2021**, *9*, 838–850. [[CrossRef](#)]
41. Cui, M.-M.; Zhang, X.; Liu, K.-G.; Li, H.-B.; Gao, M.-M.; Liang, S. Fabrication of nano–grained negative temperature coefficient thermistors with high electrical stability. *Rare Met.* **2021**, *40*, 1014–1019. [[CrossRef](#)]

Disclaimer/Publisher’s Note: The statements, opinions and data contained in all publications are solely those of the individual author(s) and contributor(s) and not of MDPI and/or the editor(s). MDPI and/or the editor(s) disclaim responsibility for any injury to people or property resulting from any ideas, methods, instructions or products referred to in the content.